Classification:
Biological Sciences; Biophysics and Computational Biology
Physical Sciences; Chemistry

Nanoscale imaging reveals laterally expanding antimicrobial pores in lipid bilayers

Paulina D Rakowska[*,†,¶¶], Haibo Jiang[‡,¶¶], Santanu Ray[*,¶¶], Alice Pyne[*,§], Baptiste Lamarre[*], Matthew Carr[¶], Peter Judge[‖], Jascindra Ravi[*], Ulla IM Gerling[**], Beate Koksch[**], Glenn Martyna[††], Bart W Hoogenboom[§,‡‡], Anthony Watts[‖], Jason Crain[*,¶], Chris RM Grovenor[‡], Maxim G Ryadnov[*,¶,§§]

[*] National Physical Laboratory, Hampton Road, Teddington, TW11 0LW, UK
[†] Department of Chemistry, University College London, WC1H 0AJ, UK
[‡] Department of Materials, University of Oxford, Parks Road, Oxford, OX1 3PH, UK
[§] London Centre for Nanotechnology, University College London, London WC1H 0AH, UK
[¶] School of Physics and Astronomy, University of Edinburgh, UK EH9 3JZ, UK
[‖] Department of Biochemistry, University of Oxford, Parks Road, Oxford, OX1 3PH, UK
[**] Institut für Chemie und Biochemie, Freie Universität Berlin, Takustrasse 3, 14195 Berlin, Germany
[††] IBM T.J. Watson Research Center, Yorktown Heights, New York, 10598, USA
[‡‡] Department of Physics and Astronomy, University College London, WC1E 6BT, UK

Abstract

Antimicrobial peptides are postulated to disrupt microbial phospholipid membranes. The prevailing molecular model is based on the formation of stable or transient pores though direct observation of the fundamental processes is lacking. By combining rational peptide design with topographical (atomic force microscopy) and chemical (nanoscale secondary ion mass spectrometry) imaging on the same samples, we show that pores formed by antimicrobial peptides in supported lipid bilayers are not necessarily limited to a particular diameter, nor they are transient, but can expand laterally at the nano-to-micrometer scale to the point of complete membrane disintegration. The results offer a mechanistic basis for membrane poration as a generic physicochemical process of cooperative and continuous peptide recruitment in the available phospholipid matrix.

\body

Structurally compromised phospholipid membranes can lead to premature cell death, which is particularly critical for unicellular microorganisms (1, 2). Multicellular organisms take the full advantage of such vulnerability by employing host defence or antimicrobial peptides (AMPs) (1-6). Although there are >1000 AMPs known to date (7), only a few, a fraction of this number, have been studied to shed light on molecular mechanisms of action. The proposed barrel-stave pore (4, 8), torroidal pore (3) and carpet models (9) differ from one another by the ways AMPs interact within phospholipid bilayers, with all these models believed to involve two distinct peptide-lipid states; an inactive surface-bound or S-state and a pore-like I-state (1, 10, 11). However, the link between these two states and membrane disintegration remains unresolved.

Despite their apparent diversity in structure and modes of action AMPs share common features, which make their modulation in model sequences possible. The peptides preferentially target anionic microbial surfaces, upon binding to which (S-state) they partition polar and hydrophobic residues by adopting amphipathic conformations (2, 12, 13). Neutron diffraction and solid-state NMR spectroscopy suggest that these amphipathic conformations assemble into perpendicular stacks that close into the pore-like structures of the I-state (5, 11, 14). Here, positive curvature strains (15) and membrane thinning (16) are induced and may precede poration. In lipid vesicles (17, 18) and supported bilayers (16) kinetic studies have implied the formation of transient pores (6) suggesting that antimicrobial peptides may expand through the monolayers of the lipid bilayers (15-18). Much research has focused on small and stabilized pores (5, 14, 15, 17). Growth arrest and uniform sizes of pores conform to the functional and structural basis of specialized transmembrane proteins, but may not be consistent with that of antimicrobial peptides. Indeed, bacterial protein toxins such as α-hemolysins oligomerize into small 2-4 nm pores of defined structure which is sufficient to cause the rapid discharge of life-supporting resources (ions, ATP) from host cells (19, 20). Cell death in this case is a consequence, but not an aim. In contrast, AMPs are designed to kill microbial cells, not necessarily specifically (21), but rapidly within the time limits of their proteolytic stability. The behaviour of other protein toxins is somewhat similar to these two scenarios. For example, perforins (22) that activate intrinsic suicide programs (apoptosis) of various cells, thus mediating cell lysis rather than causing it directly, employ different avenues for membrane targeting and can form heterogeneous transmembrane pores (23). Heterogeneity in pore formation for AMPs may derive from that, unlike the case of all membrane proteins (24), there are no a priori topological constraints on assembled structures that the peptides must adopt in bilayers. Therefore, their pore sizes may be governed as much by progressive peptide aggregation as they are by local energetics. Because AMPs are typically cationic free-energy changes in the edges of pores can be affected by peptide positions and local variations in a dielectric medium between peptide molecules suggesting strong electrostatic repulsion. In this light, poration can be described as a physical phenomenon accommodating peptide diffusion in the membrane matrix with no strict predisposition for a particular pore size, but with sufficient freedom of movement for lateral expansion. To address this in a sufficient molecular detail, the direct observation of pore architecture and dynamics is needed, but thus far has been lacking.

One reason for this is the intrinsic complexity of imaging poration in live cells. Membrane binding of AMPs is kinetically driven and, in live cells, occurs over timescales of microseconds to minutes (2, 25). Pores need not expand substantially because cell death can occur concomitantly as a result of membrane leakage and swelling under osmotic pressure and because AMPs can reach and bind to intracellular targets or disrupt processes that are crucial to cell living (protein, DNA or cell wall syntheses) within the same timescales (2, 25). Further, microbial membranes are 3D architectures whose diameters do not exceed two microns. Pore formation in these membranes relates to increased surface tension which can lead to “premature” membrane rupture before individual pores can expand substantially. A visible expansion in live cells depends on these inter-related factors, which makes its direct observation problematic.

In contrast, longer time and length scale studies are accessible in supported lipid bilayers (SLBs) (26). SLBs provide ideal experimental models for fluid-phase membranes and can be imaged by atomic force microscopy (AFM) (27, 28). Combining AFM with high-resolution secondary-ion mass spectrometry (SIMS), which has been shown to provide compositional chemical imaging of small lipid domains with lateral resolution of <100 nm (29), permits the detailed visualization of poration in SLBs.

To mitigate the complexities of direct live cell studies we introduce and explore here a model system designed to expose the fundamental physicochemical processes relevant in the peptide-bilayer interactions. A model antimicrobial peptide, which combines main features of helical AMPs, was designed to integrate into SLBs that were then used as substrates for detailed nanoscale imaging and analysis by AFM and high resolution SIMS.

Results

To enable pore formation, a de novo amino-acid sequence, KQKLAKLKAKLQKLKQKLAKL, dubbed amhelin (*a*nti*m*icrobial *hel*ix *in*sert), was generated as an archetypal model of transmembrane AMPs. The peptide comprises three *PPPHPPH* heptads, in which *P* is polar or small (alanine) and *H* is hydrophobic. This arrangement allows for the formation of a contiguous amphipathic helix in SLBs spanning ~3.15 nm (0.54 nm per turn) to match the bilayer thickness of ~3.2 nm (30, 31). The heptads in the sequence place *i* and *i+7* residues (32), which are of the same type, next to each other when viewed along the helical axis (Fig. 1A and Fig. S1 in Supporting Information). This ensures the segregation of hydrophobic and polar residues onto distinct regions or faces giving rise to an amphipathic helix. The hydrophobic face was kept short at the 1:1.5 ratio of hydrophobic (leucine) to cationic (lysine) residues to avoid hemolytic activities common for venom peptides that have broader hydrophobic clusters (4, 33). To support the ratio, small alanines and neutral glutamines, which do not contribute to membrane binding, were alternately arranged in the polar face as a neutral cluster opposite to the hydrophobic face (see also Supporting Information).

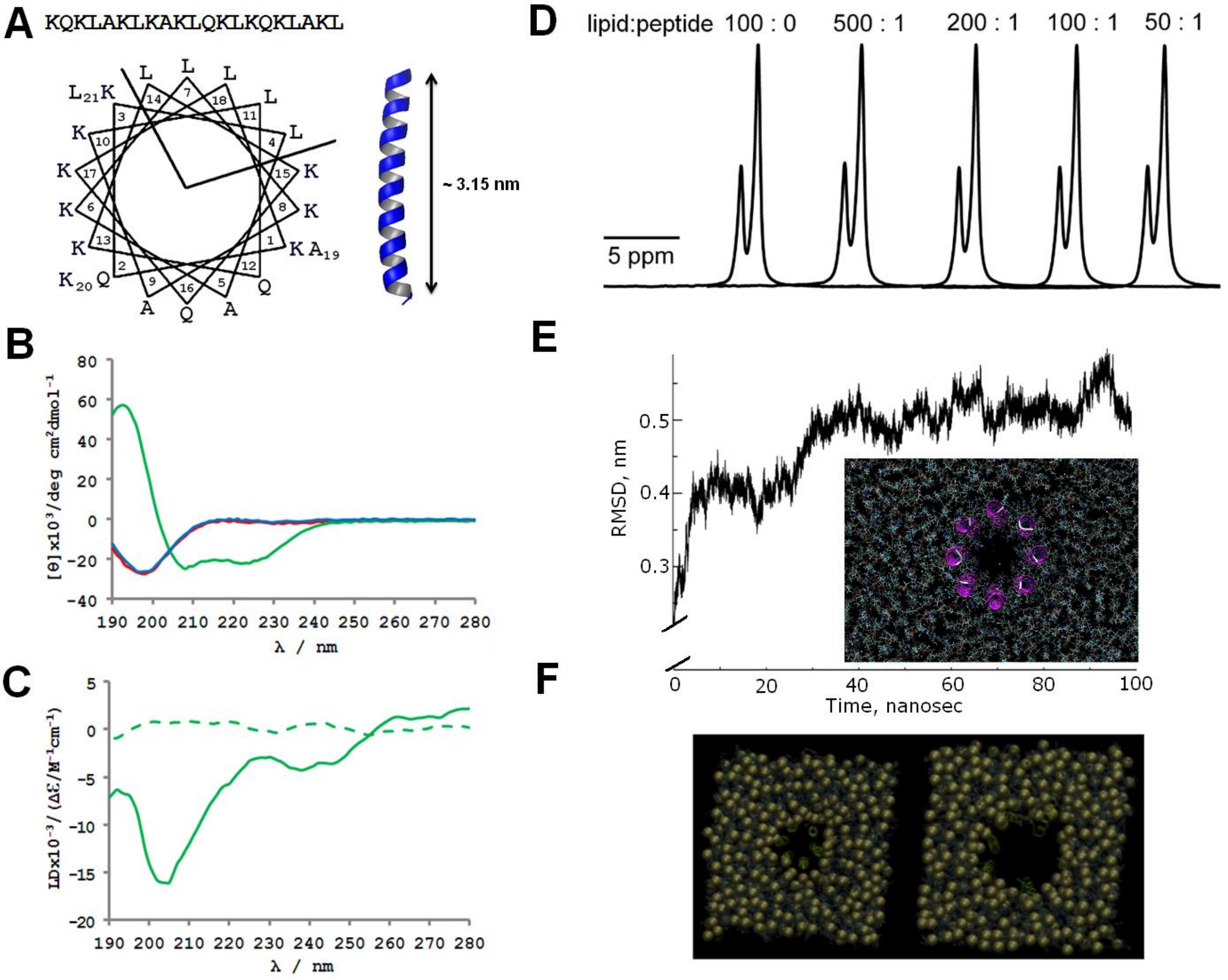

Figure 1. Peptide design and folding. (A) amhelin sequence, linear and on a helical wheel, and as an amphipathic helix spanning ~3.15 nm (in blue, 2ZTA PDB entry rendered with PyMoL). (B) CD spectra of amhelin (20 μM) in 10 mM phosphate buffer (red line), ZUVs (blue line) and AUVs (green line). (C) LD spectra of amhelin (solid line) and the non-AMP (dashed line) (both at 20 μM) in AUVs. (D) ^{31}P MAS ssNMR spectra of AUVs mixed with amhelin at different lipid-peptide ratios, -0.9 ppm (large peak) and 0.2 ppm (small peak) resonances arise from the PC and PG headgroups, respectively. (E) RMSD for the molecular dynamics simulation of a model octameric amhelin pore (initial configuration in inset) in an AUV bilayer. (F) Initial (left) and later stage (right) configurations of a model hexameric amhelin pore in the bilayer.

Peptide folding in solution was probed using zwitterionic unilamellar vesicles (ZUVs) and anionic unilamellar vesicles (AUVs) mimicking mammalian and microbial membranes respectively (33, 34). Dilauroylphosphatidylcholine (DLPC) was used to assemble ZUVs, whereas its mixtures with dilaurylphosphatidylglycerol (DLPG) at 3:1 ratios were used to assemble AUVs (30, 33). These lipid compositions yield fluid-phase membranes at room and physiological temperatures (27, 30, 31). Circular dichroism (CD) spectroscopy revealed that amhelin did not fold in aqueous buffers or in the presence of ZUVs at micromolar concentrations. In contrast, an appreciable helical signal was recorded for the peptide in AUV samples (Fig. 1B). Linear dichroism (LD) spectroscopy, which gives a convenient probe for relative peptide orientation in membranes, showed band patterns comprising maxima at 190-195 nm and 220-230 nm, and a minimum at 205-210 nm, which are indicative of peptide insertion into AUVs in a transmembrane manner (Fig. 1C) (35). In contrast, no LD signal was observed for a designed non-AMP, which cannot bind and order in membranes (Fig. 1C) (33, 36). ^{31}P MAS solid state NMR (ssNMR) spectra of AUV mixed with amhelin revealed increasing broadening of phospholipid peaks as a function of decreasing lipid-peptide ratios (Fig. 1D). This broadening effect relates to an increase in linewidth caused by a decrease in the T2 relaxation time (37), which corresponds to an increase in correlation time of the phospholipid groups. This suggests a decrease in motion of phospholipid groups in contact with the peptide, which is more pronounced at higher peptide concentrations and is more noticeable in thicker and less fluid membranes (Fig. S1). Taken together this is consistent with a transmembrane insertion of the peptide.

Early oligomers of helical inserts are believed to arrange into small pores whose projections can be obtained by crystallizing peptide-lipid assemblies in fluid bilayers as a function of hydration and temperature (14). Diffraction patterns of such assemblies show regular hexagonal arrays of pores comprising just a few helices. To probe the dynamics of poration and expansion, amhelin inserts in AUVs were explored with molecular dynamics simulations using the CHARMM36 force field (36). Amhelin helices remained stable with slightly tilted orientations over timescales of 100 ns (Video S1), whereas rudimentary hexameric and octameric pores constructed in the bilayers expanded with the root-mean-square displacement (RMSD) separations doubling in diameter over timescales of order 100 ns (Fig. 1E, 1F and Video S2). This implies that early oligomers have a tendency for expansion, which may occur at the expense of further peptide recruitment in the pores.

Consistent with the folding and simulation data, amhelin exhibited antimicrobial activity with minimum inhibitory concentrations typical of AMPs, while showing negligible hemolytic activity (Table S1 and Fig. S2) (1, 2, 12, 21). AFM revealed the surface corrugation of amhelin-treated bacterial cells (*E. coli*) (Fig. S2). The analysis of pore-like structures was deemed ambiguous due to the considerable roughness of the cell surfaces (Fig. S2) (25). A comparative analysis was performed on SLBs prepared by the surface deposition of AUV in aqueous solution using adapted protocols (26, 29). Silicon wafers used as substrates were coated with a 9-nm layer of silicon dioxide to (i) support homogeneous and stable bilayers maintained in the fluid phase at room temperature and (ii) avoid charge build-up during SIMS measurements, which is necessary as SIMS relies on the detection of secondary ions extracted from the surface by a focused beam of primary ions (^{133}Cs^{+}) rastered across the sample (29).

The SLB samples were incubated with solutions containing amhelin, which was ^{15}N-labeled at all alanine and leucine residues, and washed to remove excess peptide. To arrest poration and preserve structural changes in the membrane, the hydrated samples were then rapidly frozen and freeze-dried (29). Secondary ion images of the ^{12}C^{14}N^{-} and ^{12}C^{15}N^{-} signals, which are commonly used in imaging SIMS experiments of biological materials (38) revealed pores of varied forms and sizes supporting the conjecture of pore expansion across the whole scanned area (Fig. 2A and Fig. S3).

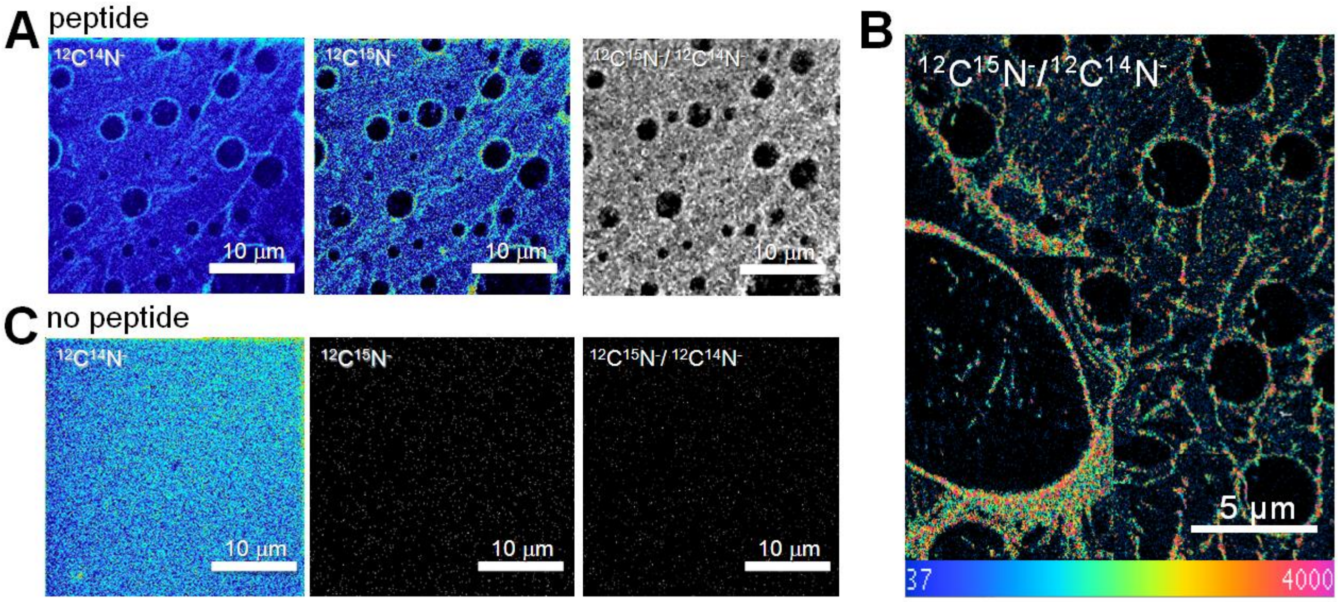

Figure 2. SIMS analysis of amhelin-treated supported lipid bilayers. (A) SIMS images of $^{12}C^{14}N^{-}$, $^{12}C^{15}N^{-}$, and $^{12}C^{15}N^{-}/^{12}C^{14}N^{-}$ signals from the supported lipid bilayers treated with the isotopically labeled peptide. (B) $^{12}C^{15}N^{-}/^{12}C^{14}N^{-}$ ratio expressed as hue saturation intensity images. The rainbow scale changes from blue (natural abundance ratio of 0.37%) to red (40%, >100 times the natural ratio). This image is the sum of several sequential images to enhance the statistical significance of the measured ratios. (C) SIMS images of $^{12}C^{14}N^{-}$, $^{12}C^{15}N^{-}$,and $^{12}C^{15}N^{-}/^{12}C^{14}N^{-}$ signals from the supported lipid bilayers with no peptide. Incubation conditions: 10 µM, pH 7.4, 20 °C.

In these samples, we expect a higher signal intensity from regions of the surface rich in peptide since each unlabeled residue in amhelin contributes to $^{12}C^{14}N^{-}$, but the $^{12}C^{15}N^{-}$ signals will come predominantly from the labeled residues. Thus, SIMS images have a strong degree of component-specificity providing direct evidence for the location of the peptide which prompts the conclusion that the observed pores are peptide-specific. This was reinforced by the images of the $^{12}C^{15}N^{-}/^{12}C^{14}N^{-}$ ratio and hue saturation intensity (HSI) images (Fig. 2B and Fig. S3). Complementary images of control samples (bare and non-AMP-treated SLBs, bare and amhelin-treated silicon wafer substrates) were featureless (Fig 2C and Fig. S4 and S5).

Firstly, all these images suggest that the interior of the pores in the amhelin-exposed samples is completely free of peptide, as are the control samples, as expected. Secondly, $^{12}C^{15}N^{-}/^{12}C^{14}N^{-}$ ratios far above natural abundance values (0.37%) are recorded from the surface of the sample away from the pores, and are particularly evident at the edges of the pores, where the peptide content appears to be highest (40%) and increases with increasing pore sizes (Fig. 2B). Thirdly, high peptide accumulations can be seen running across the NanoSIMS images, presumably pore-connecting ridges which are spread across the imaged area suggesting peptide migration dynamics (Fig. 2A, 2B and S3).

It should be emphasized here that SIMS measurements relate to the chemical composition of the surface with only a minor contribution from topography. Therefore, AFM measurements on the same samples were performed to support the SIMS data (Fig. 3). AFM-scanned pore sizes revealed that the pore edges protruded from the surface to the heights of ~4 nm (Fig. 3A). The long axis of the peptide can account for ~3.2 nm, whereas the remaining is consistent with the size of the head of a displaced lipid, which can be free or peptide bound (Fig. 3B). Although viewed as aligned in the pore edges (4, 5) the peptides could also stagger with every other peptide being shifted slightly upward (Fig. 3B). In addition, small white-dot deposits observed predominantly inside the pores and on their edges are most likely due to the aggregation of peptide-lipid material ejected from the membrane. This altogether (i) suggests that the peptide incorporates into the bilayer by distorting and partially displacing the lipids of the outer leaflet and (ii) implies an efficient migration mode of lipid-peptide assemblies through fluidic pores and ridges in a highly cooperative manner.

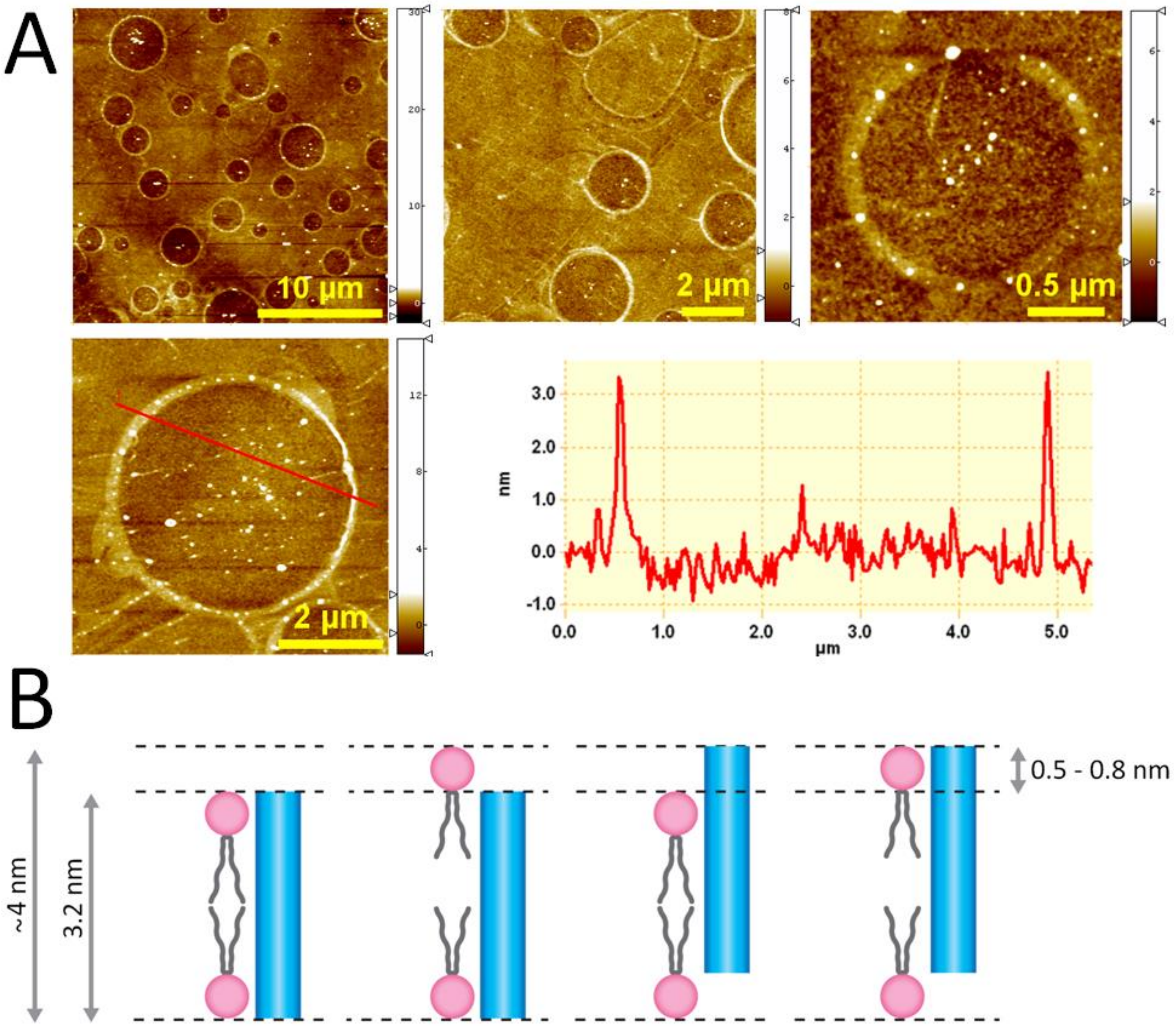

Figure 3. Amhelin-treated supported lipid bilayers. (A) In-air AFM topographic images with a cross section along the highlight line. (B) Schematic representation of pore edges showing the thickness of the SLB (3.2 nm), the maximum observed height (4 nm) and the difference between the two (0.5-0.8 nm) accounted for by three possible protrusion variants shown. For clarity only one peptide (blue cylinder) and one phospholipid per layer are shown (aliphatic chains in grey, headgroups in pink). Incubation conditions: 10 µM, pH 7.4, 20 °C.

An intriguing question provoked by the observations is the peaking of pore edges. Although the heights of the edges were fairly consistent, the depth values of the perforations could not be determined reliably. The holes would appear as deep as ~2 nm in relation to the surrounding surfaces, but an explicit cross-section analysis was hampered by high noise levels from the surfaces in the 1-2 nm range. The peaking itself may become negligible under equilibrium conditions at which outer leaflet lipids detach irreversibly and too fast to be observed without deliberately arresting the system by freezing. An insight into this can be obtained only in solution.

With this in mind we monitored real-time changes of SLBs incubated with amhelin by time-lapse AFM in water (25). Amhelin solution at low concentration was directly introduced into a liquid cell which contained an AUV lipid bilayer assembled on flat mica. After the first 10 min of incubation small pores started forming on the surface and continued to grow in size and numbers over the period of 2 hours culminating in the total removal of the lipid from the mica surface (Fig. 4A). The lipids are likely to dissolve in the form of micelles, possibly including peptides. On removal of larger amounts of the SLB, material increasingly precipitates on the surface (Fig. 4A and Fig. S6). As expected, the pores appeared as expanding holes suggesting the displacement of outer lipids from the surface into the water, which is characteristic of equilibrated systems (17). The depths of perforations reached ~2.7 nm conforming to the amhelin spanning the bound hydrophobic core of the bilayer (Fig. 4B).

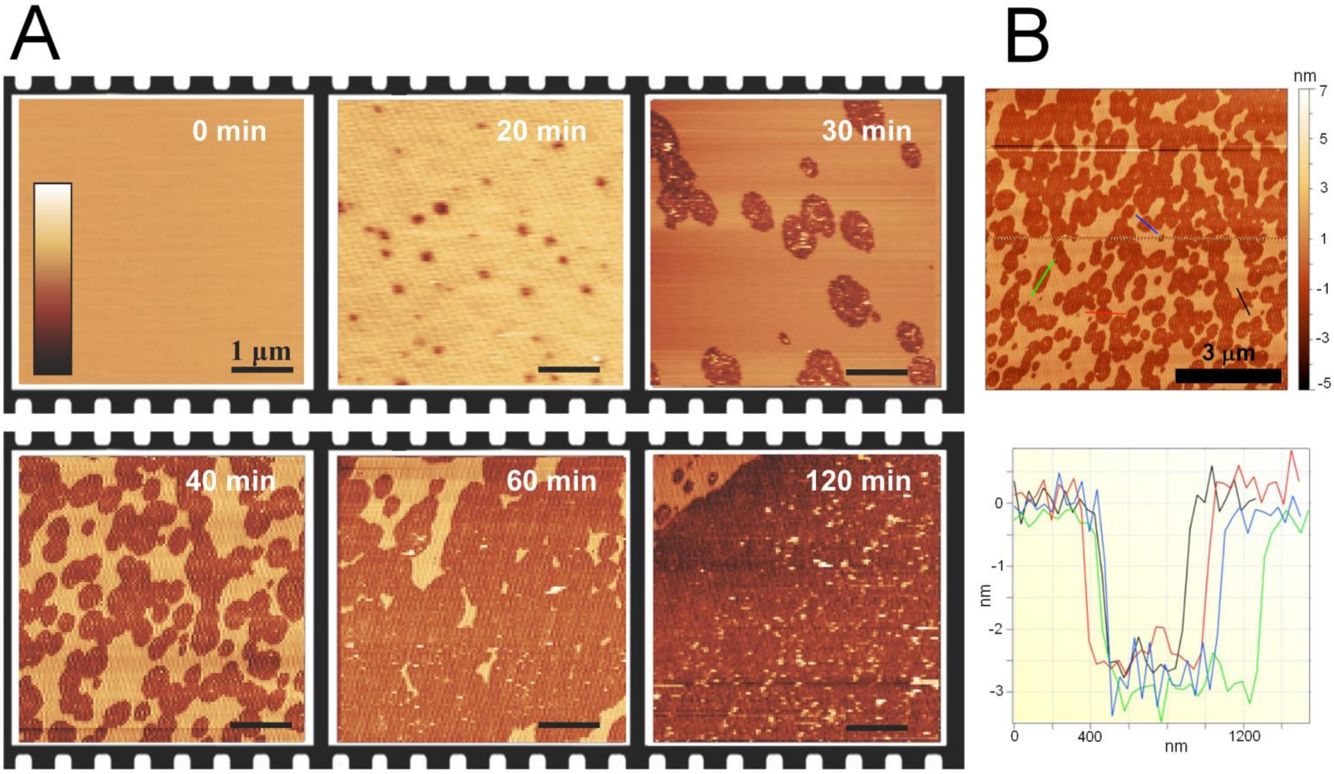

Figure 4. In-water AFM imaging of amhelin-treated supported lipid bilayers. (A) Topography of supported lipid bilayers during incubation with amhelin. Color scale (see inset, 0 min): 3 nm (0-20 min); 9 nm (30-120 min). (B) Topography image after 40 min incubation with cross sections along the highlighted lines. Incubation conditions: 0.5 µM, pH 7.4, 20 °C.

Discussion

Collectively our findings provide evidence for pore expansion, or an E-state, of amphipathic antimicrobial peptides in lipid bilayers (Fig. 5). The E-state promotes cooperative peptide migration through the lipid matrix and can persist to complete membrane disintegration. Our proposed model of pore expansion is the synergistic interplay of two physical processes.

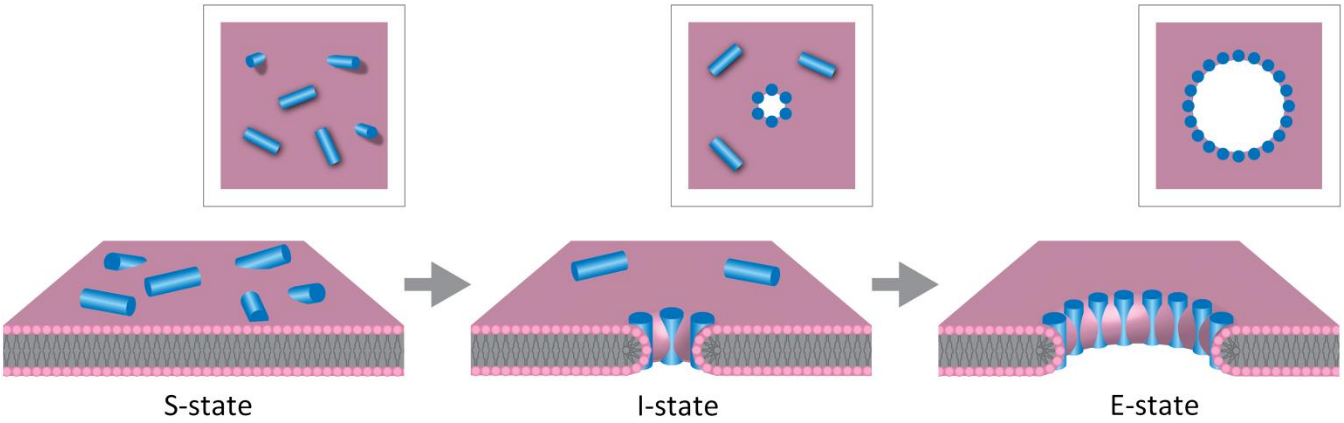

Figure 5. Proposed pore expansion mechanism for amphipathic antimicrobial peptides. Antimicrobial peptides (blue cylinders) bind to the surface of the membrane (S-state), insert into lipid bilayers forming pores (I-state), which can then expand indefinitely (E-state).

In the first, peptide adsorption induces surface tension on membrane surfaces which when sufficiently large leads to poration. The pore formation promotes peptide migration from the surface to the edges of the pores. This variation of surface tension with composition (Gibbs surface excess) is driven by amphipathic peptides having higher affinity to the membrane edges (33). The process is likely to reduce the tension between peptide and lipid bilayers thereby stabilizing the formed pores. However, it is challenged by strong electrostatic repulsion between inserted helices in the pore edges (34). In live cells this conflict can be avoided both because excess peptide on cell membranes can migrate through small pores directly into the cytoplasm targeting intracellular components and because continuous peptide incorporation and diffusion in lipid bilayers can be preempted by membrane swelling (6, 12, 22). For flat and extended 2D lipid matrices pore expansion is more thermodynamically favourable and is determined by both incorporation and repulsion of peptides to the pore edges. In this way, inserting helices can be viewed as charged equipotential surfaces with a degree of translational freedom (33) conforming to toroidal type poration which is characterized by shallow energy minima leading to substantial variations in pore sizes (34).

Pores of 10 μm in size can be physically generated in giant unilamellar vesicles (100 μm in diameter) by strong optical illumination in a viscous medium (35). The edges of the generated pores make up a “line” of lipid bilayer edges which, unless stabilized or expanded, reseal due to the “line” tension (33). Detergent molecules (e.g. Tween 20) can reduce the tension and partially stabilize the line (16, 35), but cannot fold and propagate. Instead, they form micellar aggregates above a critical concentration. In contrast, antimicrobial peptides become amphipathic only upon folding which in conjunction with sustained hydrophobic and electrostatic interactions enables their progressive self-assembly in lipid bilayers. Pore expansion is also different from mechanisms of fusion and transmembrane proteins whose conserved topologies impose specific self-assembly modes and pore architectures (18). For example, HIV gp41 controls each step in fusion including pore nucleation through a sequence of highly specialized conformations rendering the dimensions and lifetime of induced pores precisely optimized for viral entry (36).

Thus, our findings support the biological rationale of antimicrobial peptides as non-specific and fast-reacting molecules that target microbial membranes and whose action depends on concentration and matrix availability rather than on pore uniformity and global structural parameters such as folding topology.

Methods

Peptide design and synthesis. Amhelin and a non-AMP control, QIAALEQEIAALEQEIAALQ and AMP2 were designed, synthesized and characterized according to protocols published elsewhere (33) (see also Supporting Information). ^{15}N-amhelin labeled at all alanine and leucine residues was purchased from AnaSpec. All peptides were identified by reverse phase high performance liquid chromatography (RP-HPLC) and MALDI-ToF mass-spectrometry.

MS $[M+H]^+$: amhelin – m/z 2448.2 (calc), 2447.7 (found); non-AMP – m/z 2152.4 (calc.), 2152.4 (found); ^{15}N-amhelin – m/z 2458.2 (calc.), 2458.1 (found); AMP2 – 2319.1 m/z (calc.), 2320.1 (found); $[M+Na]^+$ and $[M+K]^+$ were also found.

Circular and linear dichroism spectroscopy. All CD spectra were recorded on a JASCO J-810 spectropolarimeter fitted with a Peltier temperature controller. All measurements were taken in ellipticities in mdeg and converted to molar ellipticities ([θ], deg cm^2 dmol^{-1}) by normalizing for the concentration of peptide bonds. Aqueous peptide solutions (300 μL, 20 μM) were prepared in filtered (0.22 μm) 10 mM phosphate buffer, pH 7.4. CD spectra recorded in the presence of synthetic membranes are for lipid:peptide molar ratio of 100:1. Solution-phase flow LD spectra were recorded on a Jasco-810 spectropolarimeter using a photo-elastic modulator 1/2 wave plate, and a micro-volume quartz cuvette flow cell with ~0.25 mm annular gap and quartz capillaries (all from Kromatec Ltd, UK). Molecular alignment was achieved through the constant flow of the sample solution between two coaxial cylinders – a stationary quartz rod and a rotating cylindrical capillary. LD spectra were acquired with laminar flow obtained by maintaining the rotation speed at 3000 rpm and processed by subtracting non-rotating baseline spectra. LD spectra recorded in the presence of synthetic membranes were prepared at a lipid:peptide molar ratio of 100:1 (2 mM total lipid, 20 μM peptide).

Solid state NMR spectroscopy. ssNMR experiments were carried out on a Varian Infinityplus 500 MHz spectrometer equipped with a 4 mm MAS HXY probe at 30°C. ^{31}P ssNMR spectra were acquired at 202 MHz. A single 4 μs 90° pulse was used to excite directly the ^{31}P nuclei, and broadband proton decoupling of 20 kHz was applied during the acquisition period. Samples were rotated at 8 kHz MAS at 20 °C. 8k scans were collected and the pulse delay was 4 s. Spectra were referenced to $NH_4H_2PO_4$.

Molecular dynamics simulations. Molecular dynamics simulations were performed using the CHARMM36 force field using chloride counter ions for charge neutralization. The initial helical configuration was obtained using the XPlor-NIH structure determination algorithm (http://nmr.cit.nih.gov/xplor-nih/). DLPC/DLPG (3:1) membranes were constructed with dimensions of 12x12nm and simulated with a semi-isotopic NPT ensemble with equilibrations of 20ns. Production runs were then performed for approximately 100ns.

In-air atomic force microscopy imaging. Topographic, amplitude and phase AFM images were recorded using tapping mode AFM on an MFP-3D Asylum AFM instrument (for imaging bacteria) and on a Cypher Instrument (Asylum Research, UK) (for imaging supported lipid bilayers). All AFM images were flattened with a first order line-wise correction fit. AFM tips used were super-sharp silicon probes (Nanosensors, Switzerland, resonant frequency ~330 kHz, tip radius of curvature <5 nm, force constant 42 N/m). Images were processed using proprietary SPIP software, version 5.1.3.

In-water atomic force microscopy imaging. Topographic images of supported lipid bilayers in liquid were recorded on a JPK Nanowizard I AFM, mounted on an Olympus IX71 inverted optical microscope, and operated in contact mode. The AFM probes used for all experiments in liquid were MSNL Silicon Nitride probes with spring constants of 0.005-0.03 N/m (Bruker AFM probes, CA, USA). Images were processed using Gwyddion (http://gwyddion.net/) first-order line-wise flattening and cross-section measurements.

High resolution secondary ion mass spectrometry. SIMS images of chemical and isotopic distributions were acquired on a CAMECA (Gennevilliers) NanoSIMS 50 with lateral resolution down to 50 nm. The instrument uses a 16 keV primary $^{133}Cs^+$ beam to bombard the sample surface and collects five selected secondary negative ions using a Mauttach-Herzog mass analyzer with electrostatic sector and asymmetric magnet configuration. $^{12}C^{14}N^-$ and $^{12}C^{15}N^-$ secondary ions were collected. Three of the following signals were also recorded simultaneously to give information on sample morphology; $^{12}C^-$, $^{13}C^-$, $^{16}O^-$ and $^{31}P^-$. The ratio images ($^{12}C^{15}N^-/^{12}C^{14}N^-$) (30 by 30 µm, 256 by 256 pixels) were collected with a large primary aperture to match the pixel size in the images with the incident ion beam diameter (~120 nm). A smaller primary aperture was used to achieve higher lateral resolution images (10 by 10 µm). The data was collected without preliminary $^{133}Cs^+$ implantation to avoid sputtering away the thin samples. The images were calculated and processed using OpenMIMS software (MIMS, Harvard University, www.nrims.harvard.edu/), were multiplied by a scale factor 10,000, and processed by a median filter with one pixel radius. Ratios of the control samples were calculated as: ratio = $^{12}C^{15}N^-/(^{12}C^{14}N^-+^{12}C^{15}N^-)\times 100\%$.

Acknowledgments

We thank Ian Gilmore and Alex Shard for their advice and support for the work. We acknowledge funding from the UK's Department of Business, Innovation and Skills, European Metrology Research Programme (HLT10), the Strategic Research Programme of the National Physical Laboratory, the Scottish Universities Physics Alliance, IBM Research, BBSRC (BB/G011729/1 to B.W.H.), EPSRC (EP/I029443/1 to J.C., EP/I029516/1 to A.W. and P.J., EP/G036675/1 to B.W.H and A.P.) and Chinese Scholarship Council (research scholarship to H.J.).

Footnotes

[¶¶] These authors contributed equally.

Author contributions: P.D.R., J.R., and U.I.M.G. performed synthetic, preparative and folding studies. H.J. performed SIMS studies. S.R. performed AFM studies. A.P. performed AFM studies in water. B.L. performed biological studies. M.C. and G.M. performed molecular dynamics simulations. P.J. performed ssNMR studies. B.K., B.W.H., A.W., J.C., C.R.M.G. and M.G.R. supervised research. M.G.R wrote the manuscript. All authors analysed data and contributed to the editing of the manuscript.

[§§] To whom correspondence should be addressed: max.ryadnov@npl.co.uk

Conflict of interest statement: The authors declare no competing financial interests.

Associated content: Supporting Information

References

1. Zasloff M (2002) Antimicrobial peptides of multicellular organisms. *Nature* 415(6870):389-395.
2. Fjell CD, Hiss JA, Hancock REW, & Schneider G (2012) Designing antimicrobial peptides: form follows function. *Nat Rev Drug Discov* 11(1):37-51.
3. Matsuzaki K, Murase O, Fujii N, & Miyajima K (1996) An Antimicrobial Peptide, Magainin 2, Induced Rapid Flip-Flop of Phospholipids Coupled with Pore Formation and Peptide Translocation†. *Biochemistry* 35(35):11361-11368.
4. Yang L, Harroun TA, Weiss TM, Ding L, & Huang HW (2001) Barrel-Stave Model or Toroidal Model? A Case Study on Melittin Pores. *Biophysical Journal* 81(3):1475-1485.

5. Qian S, Wang W, Yang L, & Huang HW (2008) Structure of transmembrane pore induced by Bax-derived peptide: Evidence for lipidic pores. *Proceedings of the National Academy of Sciences* 105(45):17379-17383.

6. Matsuzaki K, Yoneyama S, & Miyajima K (1997) Pore formation and translocation of melittin. *Biophysical Journal* 73(2):831-838.

7. Fjell CD, Hancock REW, & Cherkasov A (2007) AMPer: a database and an automated discovery tool for antimicrobial peptides. *Bioinformatics* 23(9):1148-1155.

8. He K, Ludtke SJ, Worcester DL, & Huang HW (1996) Neutron scattering in the plane of membranes: structure of alamethicin pores. *Biophysical Journal* 70(6):2659-2666.

9. Pouny Y, Rapaport D, Mor A, Nicolas P, & Shai Y (1992) Interaction of antimicrobial dermaseptin and its fluorescently labeled analogs with phospholipid membranes. *Biochemistry* 31(49):12416-12423.

10. Huang HW (2000) Action of Antimicrobial Peptides: Two-State Model†. *Biochemistry* 39(29):8347-8352.

11. Mani R*, et al.* (2006) Membrane-dependent oligomeric structure and pore formation of a β-hairpin antimicrobial peptide in lipid bilayers from solid-state NMR. *Proceedings of the National Academy of Sciences* 103(44):16242-16247.

12. Schmitt MA, Weisblum B, & Gellman SH (2006) Interplay among Folding, Sequence, and Lipophilicity in the Antibacterial and Hemolytic Activities of α/β-Peptides. *Journal of the American Chemical Society* 129(2):417-428.

13. Sinthuvanich C*, et al.* (2012) Anticancer β-Hairpin Peptides: Membrane-Induced Folding Triggers Activity. *Journal of the American Chemical Society* 134(14):6210-6217.

14. Yang L, Weiss TM, Lehrer RI, & Huang HW (2000) Crystallization of Antimicrobial Pores in Membranes: Magainin and Protegrin. *Biophysical Journal* 79(4):2002-2009.

15. Hallock KJ, Lee D-K, & Ramamoorthy A (2003) MSI-78, an Analogue of the Magainin Antimicrobial Peptides, Disrupts Lipid Bilayer Structure via Positive Curvature Strain. *Biophysical Journal* 84(5):3052-3060.

16. Mecke A, Lee D-K, Ramamoorthy A, Orr BG, & Banaszak Holl MM (2005) Membrane Thinning Due to Antimicrobial Peptide Binding: An Atomic Force Microscopy Study of MSI-78 in Lipid Bilayers. *Biophysical Journal* 89(6):4043-4050.

17. Lee M-T, Hung W-C, Chen F-Y, & Huang HW (2008) Mechanism and kinetics of pore formation in membranes by water-soluble amphipathic peptides. *Proceedings of the National Academy of Sciences* 105(13):5087-5092.

18. Yu Y, Vroman JA, Bae SC, & Granick S (2009) Vesicle Budding Induced by a Pore-Forming Peptide. *Journal of the American Chemical Society* 132(1):195-201.

19. Fang Y, Cheley S, Bayley H, & Yang J (1997) The Heptameric Prepore of a Staphylococcal α-Hemolysin Mutant in Lipid Bilayers Imaged by Atomic Force Microscopy†. *Biochemistry* 36(31):9518-9522.

20. Song L*, et al.* (1996) Structure of Staphylococcal α-Hemolysin, a Heptameric Transmembrane Pore. *Science* 274(5294):1859-1865.

21. Shai Y (2002) Mode of action of membrane active antimicrobial peptides. *Peptide Science* 66(4):236-248.

22. Law RHP*, et al.* (2010) The structural basis for membrane binding and pore formation by lymphocyte perforin. *Nature* 468(7322):447-451.

23. Praper T*, et al.* (2011) Human Perforin Employs Different Avenues to Damage Membranes. *Journal of Biological Chemistry* 286(4):2946-2955.

24. Shea J-E, Onuchic JN, & Brooks CL (1999) Exploring the origins of topological frustration: Design of a minimally frustrated model of fragment B of protein A. *Proceedings of the National Academy of Sciences* 96(22):12512-12517.

25. Fantner GE, Barbero RJ, Gray DS, & Belcher AM (2010) Kinetics of antimicrobial peptide activity measured on individual bacterial cells using high-speed atomic force microscopy. *Nat Nano* 5(4):280-285.
26. Mingeot-Leclercq M-P, Deleu M, Brasseur R, & Dufrene YF (2008) Atomic force microscopy of supported lipid bilayers. *Nat. Protocols* 3(10):1654-1659.
27. Lin W-C, Blanchette CD, Ratto TV, & Longo ML (2006) Lipid Asymmetry in DLPC/DSPC-Supported Lipid Bilayers: A Combined AFM and Fluorescence Microscopy Study. *Biophysical Journal* 90(1):228-237.
28. Dufrene YF (2004) Using nanotechniques to explore microbial surfaces. *Nat Rev Micro* 2(6):451-460.
29. Kraft ML, Weber PK, Longo ML, Hutcheon ID, & Boxer SG (2006) Phase Separation of Lipid Membranes Analyzed with High-Resolution Secondary Ion Mass Spectrometry. *Science* 313(5795):1948-1951.
30. Leckband DE, Helm CA, & Israelachvili J (1993) Role of calcium in the adhesion and fusion of bilayers. *Biochemistry* 32(4):1127-1140.
31. Kučerka N*, et al.* (2005) Structure of Fully Hydrated Fluid Phase DMPC and DLPC Lipid Bilayers Using X-Ray Scattering from Oriented Multilamellar Arrays and from Unilamellar Vesicles. *Biophysical Journal* 88(4):2626-2637.
32. Akerfeldt KS, Lear JD, Wasserman ZR, Chung LA, & DeGrado WF (1993) Synthetic peptides as models for ion channel proteins. *Accounts of Chemical Research* 26(4):191-197.
33. Ryadnov MG, Mukamolova GV, Hawrani AS, Spencer J, & Platt R (2009) RE Coil: An Antimicrobial Peptide Regulator. *Angewandte Chemie International Edition* 48(51):9676-9679.
34. Nomura K*, et al.* (2005) Induction of Morphological Changes in Model Lipid Membranes and the Mechanism of Membrane Disruption by a Large Scorpion-Derived Pore-Forming Peptide. *Biophysical Journal* 89(6):4067-4080.
35. Hicks MR, Kowalski J, & Rodger A (2010) LD spectroscopy of natural and synthetic biomaterials. *Chemical Society Reviews* 39(9):3380-3393.
36. Klauda JB*, et al.* (2010) Update of the CHARMM All-Atom Additive Force Field for Lipids: Validation on Six Lipid Types. *The Journal of Physical Chemistry B* 114(23):7830-7843.
37. Yeagle PL (1990) *Phosphorus NMR of membranes.* (Plenum Press, New York).
38. Moore KL, Schröder M, & Grovenor CRM (2012) Imaging Secondary Ion Mass Spectroscopy. *Handbook of Nanoscopy*, (Wiley-VCH Verlag GmbH & Co. KGaA), pp 709-744.

Supporting Information – figure legends:

Figure S1. Peptide design. (A) Linear amhelin and AMP2 sequences aligned with the repetitive heptad patterns, PPPHPPH (top) and CNCHNCH (bottom). *i, i+7* amino-acid pairs of the same type are colored. Different colors denote different pairs. *i, i+3* and *i, i+4* helical spacings are shown for N residues only for clarity. (B) Amhelin sequence configured onto an α-helical wheel with 3.6 residues per turn showing amino-acid clustering and *i, i+7* pairs (colored as in (A)). (C) ^{31}P MAS ssNMR spectra of three different AUVs mixed with amhelin at different lipid-peptide ratios. Full width half height ratios of PC and PG peaks from 100:0 to 50:1 lipid-peptide ratios show increases by 2.8% (DL), 21% (DM) and 42% (PO).

Figure S2. Antimicrobial activity of amhelin. (A) Topographic in-air AFM images of *E. coli* cells with and without amhelin including high-mag 3D images of individual cells. (B) Low-mag 3D images of bacterial cells incubated with amhelin. (C) Average number of stain-dead cells incubated with amhelin (blue) and the non-AMP, QIAALEQEIAALEQEIAALQ, (green) as a function of time. (D) Fluorescence microscopy images of PI-stained *E. coli* cells. Incubation conditions: 10 μM peptide, 30 min, at OD600nm=0.008.

Figure S3. Nano-SIMS images and line scans of supported lipid bilayers treated with ^{15}N-amhelin. The line scans plot $^{12}C^{15}N^-/^{12}C^{14}N^-$ ratios along the yellow lines in corresponding images. The natural abundance of ^{15}N is 0.37%. Image sides are 30 μm (256 x 256 pixels). Incubation conditions: 10 μM peptide, 30 min, pH 7.4, 20 °C.

Figure S4. Nano-SIMS images of supported lipid bilayers without peptide treatment. Image sides are 30 μm (256 x 256 pixels). $^{12}C^{14}N^-$ images were set to royal color scale (0-30), and $^{12}C^{15}N^-$ images were set to grey color scale (0-1). Ratios ($^{12}C^{15}N^-/(^{12}C^{14}N^-+^{12}C^{15}N^-)$) of the above images are 0.367%, 0.364%, 0.372 and 0.369% respectively. Incubation conditions: no peptide, 30 min, pH 7.4, 20 °C.

Figure S5. In-air AFM images of control surfaces. (A) Supported lipid bilayers treated with the non-AMP. (B) Bare silicon wafer substrates treated with amhelin. Incubation conditions: 10 μM peptide, 30 min, pH 7.4, 20 °C.

Figure S6. In-water AFM imaging of AMP2-treated supported lipid bilayers. The circle highlights a pore. Color scales (see insets) – from left to right, the first three are 3 nm, the last one is 8 nm. Incubation conditions: 1 μM, pH 7.4, 20 °C.